

Towards to Robust and Generalized Medical Image Segmentation Framework

Yurong Chen, *Member, IEEE*, Hui Zhang, *Member, IEEE*, Yaonan Wang, Lizhu Liu,
Q. M. Jonathan Wu, *Senior Member IEEE*, Yimin Yang, *Senior Member IEEE*

Abstract—Deep learning-based computer-aided diagnosis is gradually deployed to review and analyze medical images. However, this paradigm is restricted in real-world clinical applications due to the poor *robustness* and *generalization*. The issue is more sinister with a lack of training data. In this paper, we address the challenge from the transfer learning point of view. Different from the common setting that transferring knowledge from the natural image domain to the medical image domain, we find the knowledge from the same domain further boosts the model robustness and generalization. Therefore, we propose a novel two-stage framework for robust generalized medical image segmentation. Firstly, an unsupervised tile-wise autoencoder pretraining architecture is proposed to learn local and global knowledge. Secondly, the downstream segmentation model coupled with an auxiliary reconstruction network is designed. The reconstruction branch encourages the model to capture more general semantic features. Experiments of lung segmentation on multi chest X-ray datasets are conducted. Comprehensive results demonstrate the superior robustness of the proposed framework to corruption and high generalization performance on unseen datasets, especially under the scenario of the limited training data.

Index Terms—Image Segmentation, Transfer Learning, Representation Learning, Robustness, Generalization.

I. INTRODUCTION

AT the core bedrock of human intelligence is the character of robust generalization: we have the capability to learn a concept of things and apply it across various tasks and conditions. As Dr. Bengio talked in [1]: “*the central challenge in machine learning is that we must perform well on new, previously unseen inputs — not just those on which our model was trained*”, modern machine learning-based techniques are ambitious to replicate this phenomenon. Thanks to the development of large datasets and the high-performance

computing hardware [2][3][4], recent algorithms can capture the general-purpose visual representations which are beneficial to inference on diverse unseen samples.

However, the medical image dataset scale is always limited due to the requirement of medical experts for annotating, and patient privacy. Moreover, most existing methods are only valid under the independent and identically distributed (i.i.d) datasets assumption. If there is a domain-shift between the test data distribution and the training one, the performance dramatically degrades. Unfortunately, this condition is common in practical applications [5]. Taking the medical image segmentation task as an example, due to the different equipment protocols and variation of samples across patients, the actual distribution of the training dataset is somehow different from that of the testing set. If there is no guarantee of the model robust generalization, directly applying the trained segmentation model on unseen data would harm the performance. In addition, the information of the test data is usually inaccessible during the training phase. Therefore, it is vital to ensure that the algorithm is robust generalization even with the limited training data.

There is a global community of researchers to utilize the transfer learning technique to explore the potential of limited annotated data [7][8]. Compared with training from scratch, transfer learning generally follows the pretraining-finetuning framework to mitigate the over-fitting problem. The neural networks are usually supervised pretrained on a large yet domain-irrelevant dataset (e.g., ImageNet [3] or Places [4]), firstly. The learned representations, as initial weights, are transferred into the target task. Then, the network is finetuned with limited annotated data to perform the downstream task. With this tide, the transfer learning remarkably improves performances of the medical image analysis algorithm, such as medical image segmentation [7], lesion detection [8].

Recently, some studies consider that pretraining is not a prerequisite for training a network. For example, He et al. [9] report that the performance of using standard models trained from scratch yields similar with their ImageNet pretraining counterparts. More precisely, the pretraining only speeds up the convergence and does not contribute to the model inference capability. Therefore, we would like to investigate whether pretraining is necessary for medical image analysis tasks (Q1), such as lung segmentation from the chest X-ray. Moreover, most existing pretrained models are based on the public image dataset (ImageNet [3]). It consists of

This work is supported in part by the National Natural Science Foundation of China under Grant 61971071, Grant 62027810, in part by the National Key R&D Program of China under Grant 2018YFB1308200.

Y. Chen, H. Zhang, Y. Wang, L. Liu are with the National Engineering Laboratory of Robot Visual Perception and Control Technology, School of Robotics, Hunan University, Changsha, Hunan, 410082 CN (e-mail: chenyrong1998, zhanghui1983, yaonan, liulz@hnu.edu.cn). Corresponding author: Hui Zhang.

Q. M. J. Wu is with the Department of Electrical and Computer Engineering, University of Windsor, Windsor, Ontario, N9B3P4 Canada (e-mail: jwu@uwindsor.ca).

Y. Yang is with the Department of Computer Science, Lakehead University, Ontario, P7B 5E1, Canada, also with the Vector Institute, Toronto, M5G 1M1, Canada. (e-mail: yyang48@lakeheadu.ca).

generic object images such as cars and houses, which are quite dissimilar to the shapes of objects in medical image applications. Furthermore, medical images are gray-scale and have similar spatial structures across data. Therefore, the knowledge learned from the natural images may be inferior to transfer on the medical images, i.e., pretraining on the ImageNet [3] might provide limited or negative improvement of the medical image analysis system. Thus, it motivates us to consider the problem that is there a gap between knowledge learned from the pretraining natural image domain and the downstream medical data domain (Q2).

In this paper, we empirically compare the segmentation performance of the model that is trained from scratch and trained following the pretraining-finetuning strategy to answer the first question (Q1). Several the-state-of-art pretraining methods, including supervised classification [10], pretext tasks-based [11][12][13], and contrastive learning-based self-supervised learning [14][15][16][17] are investigated. From the experiment result, we notice that most pretraining models do not substantially improve training accuracy, however, they have a positive impact on the performance of model robustness and generalization. In this paper, the inference performance given the corrupted input data stands for the model robustness, following the research work [18]. For the generalization capability tests, we utilize three heterogeneous chest X-ray datasets that one for training, others for testing.

Under the assumption that pretraining can boost the inference performance, we continue to study the second problem (Q2). We compare models that are pretrained on the general natural image (i.e. ImageNet [3]) and pretrained on the domain-related medical data (chest X-ray images, in this paper). However, utilizing existing pretraining models, e.g. MoCo [17] on the medical image dataset is ill-conceived. First of all, training these models is time-consuming and requires a large amount of data. Secondly, these pretext tasks, such as predicting the rotation of the image, and contrastive learning strategies are inessential for the medical image. Considering that we expect the representation learned from pretraining to be general, semantic, and transferrable not detailed, trivial, and task-dependent, in this paper, we propose the Tile-wise AutoEncoder (T-AE) pretraining architecture coupled with solving the *jigsaw puzzle* as a novel pretraining method to learn the global and local representation of medical images without supervision, as shown in Fig. 1 (a). In particular, we divide an image into n^2 non-overlapping tiles. The latent feature of each tile is learned by the generative model, i.e. the sliced-Wasserstein-regularized autoencoder in this paper. Moreover, we shuffle image tiles and then train the network to reorder, in other words, solving the *jigsaw puzzle*. It encourages the network to capture more global representation and tiles context information. In addition, we leverage the decoder of the T-AE to construct the reconstruction branch of the downstream network. Both the encoder and the decoder can be transferred from the pretraining, as shown in Fig. 1 (b). The designed reconstruction task further improves the model robustness and generalization performance.

Finally, our contributions can be summarized as follows:

(i) We find that pretraining is necessary for medical image

analysis networks. Although it cannot significantly improve the model accuracy on the trained dataset, it has a positive effect on inference unseen heterogeneous domains and corrupted inputs. Moreover, we show that pretraining on the ImageNet is inferior to pretraining on the domain-related data.

(ii) We propose a simple yet effective pretraining architecture, the T-AE, to learn meaningful representations based on the domain-related data without supervision.

(iii) In the end, the downstream task, coupled with the reconstruction branch, is coined to further improve the model performance by maintaining the decodable latent feature.

Experiments are conducted on multiple chest X-ray datasets to demonstrate the generalization capability and robustness of the proposed segmentation framework. Moreover, our paper can trigger and inspire further research works.

II. RELATED WORK

A. Medical Image Segmentation

Segmentation of medical images is a fundamental part of any computer-aided diagnosis (CAD) system. Deep learning-based methods have made overwhelming achievements in this field. Recently, the segmentation network architecture designing has been attracted the interest of researchers. U-shaped convolutional neural networks (CNNs) have earned outstanding performance and become the most popular methods [20]. Motivated by the U-shaped network, a dual UNet is designed to segment the lung from cross-manufacturer chest X-ray [21]. Moreover, the DeepLab V3+ architecture [22] is proposed based on the atrous convolutions and pooling operators, and the conditional random field (CRF) post-processing technique. PSPNet [23] as the winner of the ImageNet scene segmentation challenge has received medical imaging researchers' attention. These the-state-of-art baseline segmentation methods provide the basics of further works. Rashid [24] utilizes the fully CNNs to perform lungs segmentation. A nonrigid registration-driven lung segmentation technique is introduced by Candemir et al. [25].

B. Pretraining Methods

Aside from segmentation network studies, transfer learning is widely used in medical image analysis to improve the performance [7][8], which follows the pretraining-finetuning process. Here, the pretrained model can provide a better initialization for the target task. Previous studies focus on transferring from natural images (e.g., ImageNet) to medical image analysis [2]. The neural networks, e.g., ResNet-50 [10], are pretrained for classification ImageNet [10], firstly. Moreover, unsupervised (self-supervised) learning for pretraining focuses on the problem of learning meaningful representations without expert annotations. The key part of self-supervised learning is to design a suitable pretext task. For example, Norooze et al. design solving the *jigsaw puzzles* as the pretext task [11]. Visual representations are learned with a fully convolution neural network through the process of colorizing gray-scale images [12]. The rotating angles of the whole images are designed as a supervision signal for training the network [13]. Recently, the contrastive learning, including

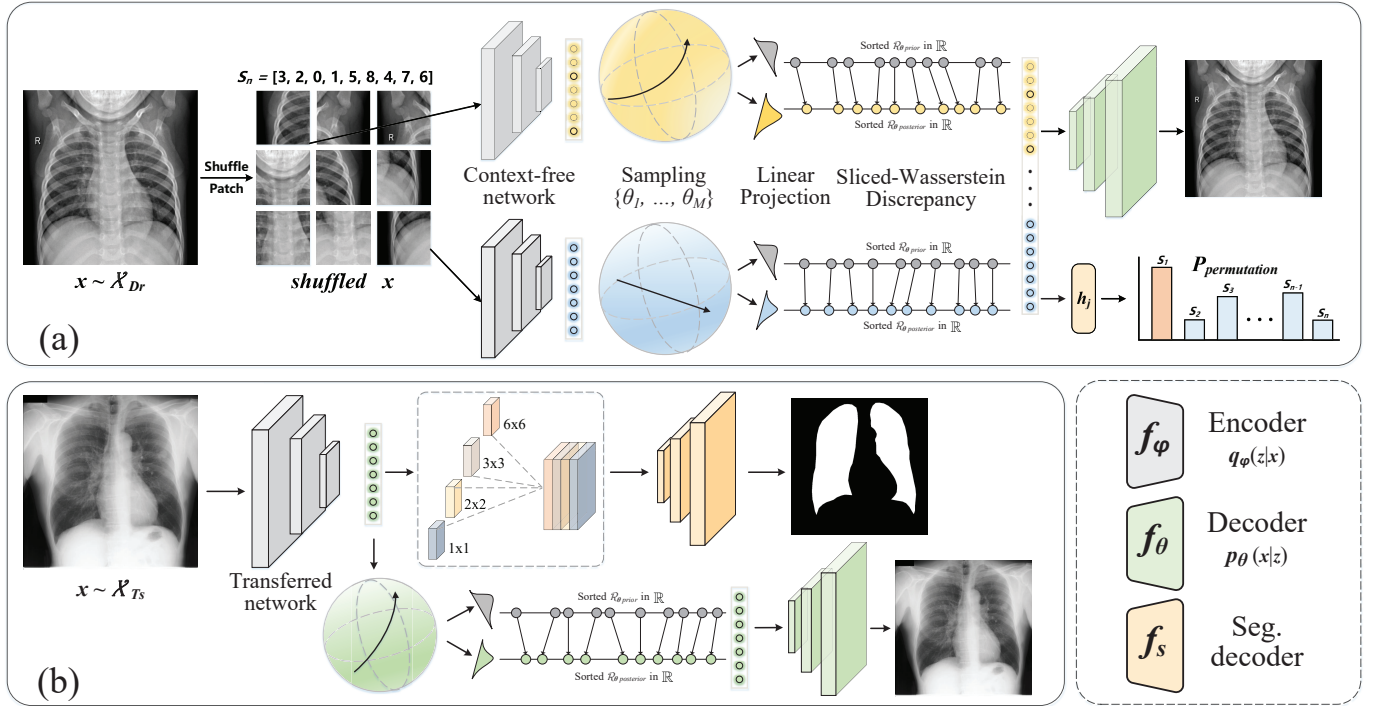


Fig. 1: Illustration of our proposed method segmentation framework, which consists of two main phases: (a) pretraining the T-AE network on domain-related (D_r) data; (b) finetuning the downstream PSPNet-based segmentation network. The encoder $f_\phi(\cdot)$ and the decoder $f_\theta(\cdot)$ are transferred from the pretraining.

SwAV [14], BYOL [15], SimCLR [16], and MoCo [17], have presented overwhelming achievements on various computer vision benchmarks. In particular, SwAV [14] introduces multi-view data augmentation and online clustering strategies into contrastive objectives. MoCo [17] leverages instance-level discrimination via momentum contrast. SimCLR [16] follows MoCo’s architecture and introduces more data augmentation methods. BYOL [15] discards negative sampling in contrastive learning. These studies mainly focus on pretraining on the domain-irrelevant data (i.e., natural general image).

C. Generative Models

Unlike contrastive self-supervised learning, generative models also have found their way to the forefront edge of representation learning in the last decade. With the development of the back-propagated-based deep learning, generative adversarial networks (GANs) [26] and Variational autoencoders (VAEs) [27] govern the generative models. GANs consist of a discriminator \mathcal{D} and a generator \mathcal{G} , which can be optimized simultaneously as a zero-sum game. Based on GANs, Cenggoro [28] proposes class expert GAN (CE-GAN) for pretraining that can mitigate the imbalanced class problem. However, GANs have innate shortcomings which are hard to train. VAEs [27], rooted in Bayesian inference, are theoretically elegant and easy to train. VAEs not only recover the data space \mathcal{X} from \mathcal{Z} , but estimate the true data distribution $p_{data}(x)$. This is a simple yet effective method to encoded the prior knowledge into the network. Motivated by this, Newell et al. [29] investigate the effect of the VAEs-pretrained model on downstream tasks.

III. METHOD

The recent medical image segmentation methods pay more attention to the model training accuracy but the model robustness and generalization. However, these performances should be more considered when applying algorithms in real-world scenarios. This paper proposes a novel robust generalized segmentation framework, which consists of pretraining on the domain-related data and finetuning on the target data. In section III.A, we formulate the problem of pretraining and medical image segmentation. Then, the proposed pretraining method is discussed in section III.B. In the end, we present the detail of the designed segmentation network in section III.C.

A. Problem Formulation and Notation

This work considers two problems: the pretraining task for learning the meaningful and transferable representations and the downstream task, i.e. lung segmentation from the chest X-ray image. Discussing in order, the pretraining task considers utilizing the domain-related dataset D_r to learn the transferable and meaningful representations. D_r is usually easy to obtain in public if we waive the need for labels. Therefore, assumes D_r including M samples ($D_r = \{x_1, x_2, \dots, x_M\}$) where $x_M \in \mathbb{R}^{H \times W \times C}$ with the height H , width W , and channel C that sampled from the domain \mathcal{X}_{D_r} in Euclidean space. The core objective of this paper is to learn a neural network, which models the data distribution of D_r (i.e., $p_{D_r}(x)$). Following the philosophy of autoencoder, we construct two neural network: an encoder (feature mapping function) $f_\phi(\cdot) : \mathcal{X}_{D_r} \rightarrow \mathcal{Z}$ and a decoder (probability estimation function)

$f_\theta(\cdot) : \mathcal{Z} \rightarrow \mathcal{X}_{Dr}$, where \mathcal{Z} is the representation space. One common strategy is that jointly train $f_\varphi(\cdot)$ and $f_\theta(\cdot)$ to reconstruct the input. In this case, the data distribution $p_{Dr}(x)$ is captured by the parameter of $f_\varphi(\cdot)$ and $f_\theta(\cdot)$. Transferring these networks to downstream can improve model performance.

For the segmentation problem, given the task-specific dataset $T_S = \{(x_1, y_1), (x_2, y_2), \dots, (x_N, y_N)\}$, where $x_N \in \mathbb{R}^{H \times W \times C}$ is the N -th independent and identically distributed (i.i.d.) input image data from the target domain manifold \mathcal{X}_{Ts} . The corresponding label $y_N \in \mathbb{R}^{H \times W \times 1}$ denotes the mask of the lung from the \mathcal{Y} . The pixel set of lung area $\{y_N^{11}, y_N^{12}, \dots, y_N^{hw}\}$ is labeled as 1 and the set of the background pixel is labeled as 0. In this paper, we utilize the fully convolutional neural network for performing segmentation. The network includes an encoder network $f_\varphi(\cdot) : \mathcal{X} \rightarrow \mathcal{Z}$ for feature extraction and a segmentation decoder network $f_s(\cdot) : \mathcal{Z} \rightarrow \mathcal{Y}$.

B. Tile-wise Autoencoder for Pretraining

In this paper, we propose a tile-wise autoencoder pretraining method, under the unsupervised learning setting. Most existing unsupervised pretraining models are based on the specific pretext task or contrastive learning. However, utilizing these algorithms on medical image data is unsuitable. For example, the gist of contrastive learning is training the network to encode the data and its' augmented version with similar representations and encode different instances with dissimilar features. Yet, different chest X-ray images might be quite similar. Considering that we expect the representation learned from pretraining to be general, semantic, and transferrable, we leverage the generative model, i.e. the autoencoder. Training the autoencoder network to fit the data distribution has an elegant theory basis [27], however, it is not easy in the medical image application. Due to the limited dataset scale, the model always has the over-fitting problem. The variational autoencoder (VAE) [27] regularizes the autoencoder with an information theory-based probability distance, which archived plenty of successes. However, utilizing the VAE [27] as the pretraining model is hampered by the over-regularization.

Here, we focus on the variational inference-based generative model and alleviate its innate challenges, furthermore, make it suitable for the domain pretraining. VAEs [27] include two main part: an inference network (i.e., encoder) $f_\varphi(\cdot)$ for modeling the posterior distribution $q_\varphi(z|x)$ and a generative network (or decoder) $f_\theta(\cdot)$ for fitting the $p_\theta(x|z)$. It can be used to estimate the true underlying distribution $p_{Dr}(x)$. The parametric inference and generative neural network can be trained jointly via maximum marginal log-likelihood $\log p_{Dr}(x)$, which equals to maximizing the evidence lower bound (ELBO) with introducing an amortized distribution $q_\varphi(z|x)$:

$$\begin{aligned} \log p_\theta(x) &\geq \mathbb{E}_{q_\varphi(z|x)}[\log p_\theta(x|z)] - D_{KL}(q_\varphi(z|x) \parallel p(z)) \\ &:= \mathcal{L}_{ELBO}(x; \theta, \varphi). \end{aligned} \quad (1)$$

As discussed in previous works [30][31], one limitation of VAEs is that the network encodes the data with collapsed features, as a consequence, the over-blurry reconstruction.

Analyzed theoretically, there are two reasons: (i) the simplistic prior distribution $p(z)$ (such as Gaussian distribution) is far to generate diverse data; (ii) the Kullback–Leibler (KL) divergence used as the regularization for approximating the inference distribution $q_\varphi(z|x)$ to the prior distribution $p(z)$ is a strong notion of distance. The fraction in log operator of the KL divergence usually takes the large gradient [30]. Therefore, the autoencoder network cannot fit the data manifold.

For mitigating the autoencoder-based pretraining problems, we propose a novel Tile-wise autoencoder (T-AE) architecture, as shown in Fig. 1. In particular, we separate the image into a regular $n \times n$ grid of tiles $x_M = \{x_M^1, \dots, x_M^k, \dots, x_M^{n^2}\}$. Each patch is assigned a prior distribution $p(z^k)$, therefore, we transform the approximating the whole image with one prior distribution into approximating the whole image with n^2 prior distributions. This is an effective yet simple technique to address the limited capability of the simplistic prior distribution. The shared weight encoder $f_\varphi(\cdot)$ can modelling each image patches. Moreover, motivated by the philosophy of the *jigsaw puzzles* that the pretext to help children learn geography [11], we introduce the solving the *jigsaw puzzles* pretext in our proposed method. Especially, beginning with $n \times n$ grid of tiles $x_M = \{x_M^1, \dots, x_M^k, \dots, x_M^{n^2}\}$, we shuffle them according to the pseudo permutation class S_i . For example, we set n to 3 and choose the permutation label $S_i = [3, 2, 0, 1, 5, 8, 4, 7, 6]$ (using python style index). The tile set is then shuffled to $x_M = \{x_M^4, x_M^3, x_M^1, x_M^2, x_M^6, x_M^9, x_M^8, x_M^5, x_M^8, x_M^7\}$. Each tile is sent to the context-free network in turn, which can be implemented with a shared weight Siamese-wise encoder $f_\varphi(\cdot)$. In the end, the final features of the image data are concatenated by the feature of each tile $\mathbb{R}^{9F} \ni z_M = [z_M^4, z_M^3, z_M^1, z_M^2, z_M^6, z_M^9, z_M^8, z_M^5, z_M^8, z_M^7]$, where $z_M^i \in \mathbb{R}^F$ is the feature of the i -th patch and F is the dimension of the latent feature. The z_M is optimized with the cross-entropy loss to predict the permutation class S_i , i.e. re-order the tiles:

$$\mathcal{L}_P = - \sum_i^N p(S_i) \log p(\hat{S}_i | z_M). \quad (2)$$

Training the autoencoder to solve the *jigsaw puzzles* endows the generative model with both local and global structure perception capability, which can further improve learning meaningful representations in the pretraining stage.

For alleviating the over-regularization problem caused by the strong notion (i.e. KL divergence), we introduce the sliced-Wasserstein distance to measure the distance between the inference posterior distribution $q_\varphi(z^k|x^k)$ and its prior $p(z^k)$. Based on but different from the p-Wasserstein distance [30]

$$W_p(p_X, p_Y) = \inf_{\gamma \in \Pi(p_X, p_Y)} \mathbb{E}_{(X, Y) \sim \gamma} [d^p(X, Y)]^{\frac{1}{p}}, \quad (3)$$

where $\Pi(p_X, p_Y)$ means the family of all joint distributions (i.e., transport maps in the optimal transport), and d is a metric function, such as the Euclidean distance $d(x, y) = \|x - y\|_2^2$, the sliced-Wasserstein distance avoids high computational cost while maintains the topology characteristic [31]. It is achieved

via the Radon transform:

$$\mathcal{R}_{p(z)}(t; \vartheta) = \int_{\mathbb{Z}} p(z) \delta(t - \vartheta \cdot z) dz, \forall \vartheta \in \mathbb{S}^{F-1}, \forall t \in \mathbb{R}, \quad (4)$$

where $\delta(\cdot)$ stands for the one-dimensional Dirac delta function and \mathbb{S}^{F-1} is the F -dimensional unit sphere. It projects the vector data into a real value. Then, the sum of the sliced-Wasserstein distance between each tile posterior distribution and its prior distribution is calculated as:

$$\mathcal{L}_{SW} = \sum_k \frac{n^2}{|\Theta|^k} \sum_{\vartheta \in \Theta^k} W_p(\mathcal{R}_{q_\varphi(z^k|x^k)}(\cdot; \vartheta), \mathcal{R}_{p(z^k)}(\cdot; \vartheta)), \quad (5)$$

where Θ denotes the set of the \mathbb{S}^{F-1} , $p(z^k)$ is the k -th patch prior distribution and can be assigned as the Gaussian distribution $\mathcal{N}(\mu^k, \sigma^{2k})$, and the \mathcal{R} is the radon transform (linear slicing) marginal distribution. In this paper, we leverage the sliced-Wasserstein distance to replace the KL divergence in the variational autoencoder, which is a weaker regularization that can maintain the data manifold and has a nice property to fit the distribution.

In conclusion, coupling with the reconstruction objective \mathcal{L}_{Rec} , such as mean squared error (MSE) $\mathcal{L}_{Rec} = \|f_\varphi(f_\theta(x)) - x\|_2^2$, the proposed pretraining method (T-AE) is trained with

$$\mathcal{L}_{T-AE} = \mathcal{L}_{Rec} + \mathcal{L}_{SW} + \mathcal{L}_P \quad (6)$$

to learn transferable and useful representations. Note that our proposed pretraining technique is a label-free method, which is more suitable to apply in the medical image analysis application. In addition, the training time is far less to most the-state-of-art pretraining models. So if the downstream segmentation network does not follow the common feature extraction backbone (e.g., ResNet-50), utilizing our proposed pretraining method is more efficient. For example, the vanilla UNet [20] tailors the architecture. Therefore, the existed pretrained model cannot be suitable and pretraining the encoder of the UNet using existing methods are time-consuming.

C. Segmentation Framework with Reconstruction Branch

Based on the common transfer learning setting, parameters of the pretrained model are utilized as the initial weights for the target task and then finetuning the network with the target data. In this section, we provide the detail of the downstream part of our proposed robust generalized medical image segmentation framework. While the deep learning-based segmentation networks have been widely developed (such as UNet [20], PSPNet [23]), in this paper, we focus on how to further improve the generalization and robustness of this architecture. Including but not limited to PSPNet and UNet, we propose a reconstruction branch incorporated with the primary task (segmentation of the lung area). The designed auxiliary task does not conflict with the primary task, meanwhile, it encourages the learned high-level features can be decoded, which can regularize the network especially when the dataset size is limited. In particular, we integrate the decoder of the

sliced-Wasserstein autoencoder which is the same setting as the proposed pretraining methods (T-AE) in the segmentation network. As discussed in the previous section, sliced-Wasserstein is a weaker notion distance compared with KL divergence. The weaker regularization is also more appropriate for the segmentation task. Therefore, parameters of both the encoder and the decoder of T-AE can be transferred into the segmentation network.

Formally, given the target domain dataset T_S including N cases, in most cases, with a limited size N , we construct a segmentation branch and a reconstruction branch. The segmentation branch consists of an encoder $f_\varphi(\cdot)$ and a segmentation decoder $f_s(\cdot)$. The reconstruction branch included a shared encoder $f_\varphi(\cdot)$ and a reconstruction decoder $f_\theta(\cdot)$. The shared encoder $f_\varphi(\cdot)$ and the decoder $f_\theta(\cdot)$ are initialized from the pretrained model then finetuned with T_S . The weight of $f_s(\cdot)$ is training from scratch with segmentation loss. Different parts of the segmentation network is jointly optimized with:

$$\mathcal{L}_{seg} = \mathcal{L}_{Dice} + \mathcal{L}_{Rec} + \mathcal{L}_{SW}, \quad (7)$$

where \mathcal{L}_{Rec} and \mathcal{L}_{SW} is the same setting as Eq. 6, and \mathcal{L}_{Dice} is a soft dice loss function [32] calculated with the segmentation decoder predict \hat{y}_N and the mask y_N .

In summary, our proposed robust generalized medical image segmentation framework consists of two stages: pretraining on the unlabeled domain-related dataset D_r to learn the general and meaningful representations via T-AE network; finetuning on the target domain dataset T_s . This transfer learning framework improves the model generalization and robustness. In the next section, we will provide the model segmentation result on the corrupted and unseen input data.

IV. EXPERIMENTS

A. Datasets

Pretraining: The pretraining dataset used for our proposed method (T-AE) should be related or the same to the target domain. In this paper, considering the segmentation lung on the chest X-ray image, we also utilize the chest X-ray (anterior-posterior) dataset for pretraining. Without loss of generality, we leverage the dataset which is similar but not the same as the target dataset. The dataset [33] including a total of 5,232 chest X-ray images, which consists of 1,349 normal cases, 3,883 characterized as depicting pneumonia. Here, we only use the 1,349 normal samples to construct the domain-related pretraining dataset D_r , and the result shows it is enough to improve the downstream task.

Target domain: Our designed medical image segmentation framework is conducted on **three** chest X-ray (anterior-posterior) datasets: Montgomery County chest X-ray set (MC) [34], Japanese Society of Radiological Technology database (JSRT) [35], and Shenzhen chest X-ray set (SH) [34]. In particular, the MC dataset contains 138 posterior-anterior x-rays. The size of the image is either 4,020 by 4,892 or 4,892 by 4,020 pixels. Furthermore, the annotated lung binary masks are provided in the dataset. The JSRT database is a publicly available dataset with 247 anterior-posterior chest X-ray gray images. The X-rays are scanned from films to a size

of 2048x2048 pixels. In each image, the lung fields have been manually segmented to provide a reference standard. SH X-ray set includes a total of 662 x-rays showing manifestations of TB. The size varies but is approximately $3K \times 3K$ pixels. The lung masks are not provided in the database, but were prepared manually by National Technical University of Ukraine ¹.

B. Experiment Setup

Implementation details: For T-AE pretraining, given the domain-related dataset during training, we first define the grid size ($n \times n$) to separate the image as tiles and the permutation pseudo-label subset S . Following the work [11], we split an image into 3 by 3 non-overlapping tiles then shuffle them according to a random permutation. Each tile is sent to the Siamese-network $f_\varphi(\cdot)$, in parallel. The $f_\varphi(\cdot)$ is implemented with the backbone of the UNet [20] or the standard ResNet-50 network of the PSPNet [23]. For each tile latent feature z_M^k , we assign a Gaussian distribution $\mathcal{N}(k, 1)$ as the prior distribution for approximating, respectively. All tiles latent features are then combined before reassembling by the flow-based warp. The auxiliary solving *jigsaw puzzle* network h_j includes one fully-connected (FC) layer to predict the permutation label. The decoder $f_\theta(\cdot)$ consists of multiple convolutional layer blocks, which include Upsample-Conv-BN-ReLU layers. We resize the input image to 624×624 . The reconstruction loss function is the mean squared error (MSE), and the objective of *jigsaw puzzle* is the cross-entropy. The optimization algorithm is the stochastic gradient descent (SGD) with an initial learning rate of 0.01 is used for the T-AE pretraining model ².

For the downstream segmentation part, we select two representative segmentation networks (PSPNet and UNet) as the baselines. The reconstruction branch is constructed with the same architecture of the decoder of the T-AE. The input images are resized to 624×624 . The reconstruction error is the mean squared error (MSE), and the segmentation objective is the dice loss function. The SGD with an initial learning rate of 0.001 is used for finetuning the segmentation network. All experiments are conducted on Pytorch library with a NVIDIA GeForce GTX 3080 GPU.

C. Results Analysis

Firstly, we compare the model segmentation performance on three target datasets (MC, JSRT, and SH). Because the lung segmentation from the chest X-ray image is an easy task, the performance of most methods can achieve a high dice metric, as shown in Table I. Here, we compare with several state-of-the-art segmentation methods, such as the DEFU-Net [21], the fully CNN [24], the anatomical atlases with nonrigid registration method [25], the DeepLab V3+ [22], the UNet [20], and the PSPNet [23]. The segmentation result is reported based on their paper [21][24][25] and on our implementation for [22][20][23]. The experiment setting follows the 5-fold cross-validation. UNet (+Ours) and PSPNet (+Ours) denote

TABLE I: Comparison lung segmentation performance on MC, JSRT, and SH dataset. Dice is utilized as the evaluation metric.

Method \ Dataset	MC	JSRT	SH
DEFU-Net [21]	95.78	/	92.27
Rashid <i>et al.</i> [24]	95.40	95.10	/
Candemir <i>et al.</i> [25]	96.10 \pm 0.8	96.70 \pm 1.8	/
DeepLab V3+ [22]	87.04 \pm 0.3	91.42 \pm 0.1	86.49 \pm 0.2
UNet [20]	89.95 \pm 0.1	94.18 \pm 0.3	88.03 \pm 0.6
PSPNet [23]	91.69 \pm 0.2	95.34 \pm 0.2	83.26 \pm 0.4
UNet (+Ours)	94.35 \pm 0.4	94.41 \pm 0.2	93.31 \pm 0.3
PSPNet (+Ours)	95.98 \pm 0.2	96.24 \pm 0.5	92.68 \pm 0.1
Rec-UNet (+Ours)	95.98 \pm 0.1	96.56 \pm 0.4	93.17 \pm 0.6
Rec-PSPNet (+Ours)	96.95 \pm 0.3	97.19 \pm 0.1	94.77 \pm 0.1

'/' denotes the result is not reported.

TABLE II: Comparison robustness performances among different data corruption in the lung segmentation task on MC dataset using UNet [20] as baseline. Dice is utilized as the evaluation metric.

Method	UNet (—)	UNet (+ VAE)	UNet (+Ours)	Rec-UNet (—)	Rec-UNet (+Ours)
Original	89.95 \pm 0.3	92.80 \pm 0.3	95.35 \pm 0.2	92.97 \pm 0.3	95.89 \pm 0.1
Gauss. Noise	71.32 \pm 0.2	90.87 \pm 0.3	89.66 \pm 0.2	81.67 \pm 0.1	93.47 \pm 0.2
Shot Noise	86.86 \pm 0.1	89.04 \pm 0.2	94.20 \pm 0.2	86.82 \pm 0.2	94.33 \pm 0.3
Impulse Noise	69.00 \pm 0.3	90.23 \pm 0.2	93.95 \pm 0.2	78.13 \pm 0.4	93.40 \pm 0.2
Speckle Noise	88.39 \pm 0.2	90.45 \pm 0.4	94.17 \pm 0.4	87.72 \pm 0.2	94.78 \pm 0.1
Poisson Noise	71.66 \pm 0.4	89.94 \pm 0.2	90.94 \pm 0.4	75.54 \pm 0.2	87.23 \pm 0.4
Dropout	87.62 \pm 0.3	92.31 \pm 0.1	93.24 \pm 0.2	89.81 \pm 0.1	94.10 \pm 0.1
Gauss. Blur	90.44 \pm 0.4	89.08 \pm 0.4	94.83 \pm 0.2	84.39 \pm 0.3	95.55 \pm 0.3
Glass Blur	88.45 \pm 0.3	89.81 \pm 0.2	94.45 \pm 0.3	91.92 \pm 0.3	95.28 \pm 0.4
Defocus Blur	89.79 \pm 0.3	89.56 \pm 0.3	94.75 \pm 0.3	88.35 \pm 0.2	95.25 \pm 0.5
Motion Blur	86.62 \pm 0.3	87.53 \pm 0.1	90.17 \pm 0.5	84.31 \pm 0.3	90.10 \pm 0.2
Zoom Blur	82.97 \pm 0.4	81.37 \pm 0.2	83.16 \pm 0.2	86.68 \pm 0.2	82.30 \pm 0.2
Fog	35.90 \pm 0.5	59.76 \pm 0.3	59.47 \pm 0.1	61.08 \pm 0.3	61.74 \pm 0.3
Contrast	25.11 \pm 0.5	20.45 \pm 0.2	58.52 \pm 0.1	23.42 \pm 0.4	63.50 \pm 0.2
Brightness	00.98 \pm 0.6	70.75 \pm 0.4	56.32 \pm 0.3	16.69 \pm 0.3	71.84 \pm 0.2
Saturate	90.44 \pm 0.4	91.14 \pm 0.1	94.19 \pm 0.1	89.48 \pm 0.2	94.67 \pm 0.3
JpegComp.	88.21 \pm 0.2	89.93 \pm 0.4	94.64 \pm 0.1	85.97 \pm 0.3	95.89 \pm 0.4
Elastic Trans.	89.52 \pm 0.2	88.65 \pm 0.2	94.68 \pm 0.3	89.39 \pm 0.2	95.95 \pm 0.1
Avg.	73.11	82.40	86.55	76.52	88.20
↓	16.84	10.40	08.80	16.45	07.69

↓ denotes that compared with the clean data (original) the average dice descent by.

using the proposed pretrained method (T-AE) as the initial weight for UNet and PSPNet, respectively. **Rec-UNet** and **Rec-PSPNet** is the UNet and PSPNet plus the proposed reconstruction branch, individually. To quantitatively analyze the performance of the proposed approach, we introduce the dice coefficient as the evaluation metric [32]. As shown in Table I, we can notice the vanilla segmentation network with our proposed method (i.e. the T-AE and reconstruction network) can achieve superior dice performance than these sophisticated methods, e.g. the **Rec-PSPNet** with T-AE pretrained model outperforms [25] by 0.85% on MC dataset and 0.49% on JSRT dataset. Moreover, both the proposed pretraining method and reconstruction branch improve performance, e.g. compared with the vanilla Unet, an improvement of 4.37% is got by UNet (+Ours) and a further improvement of 1.63% is got by

¹<https://www.kaggle.com/yoctoman/shcxr-lung-mask>

²The code is available: <https://github.com/YurongChen1998/yurong-lib/tree/main/pytorch/PSPNet.SWAE>

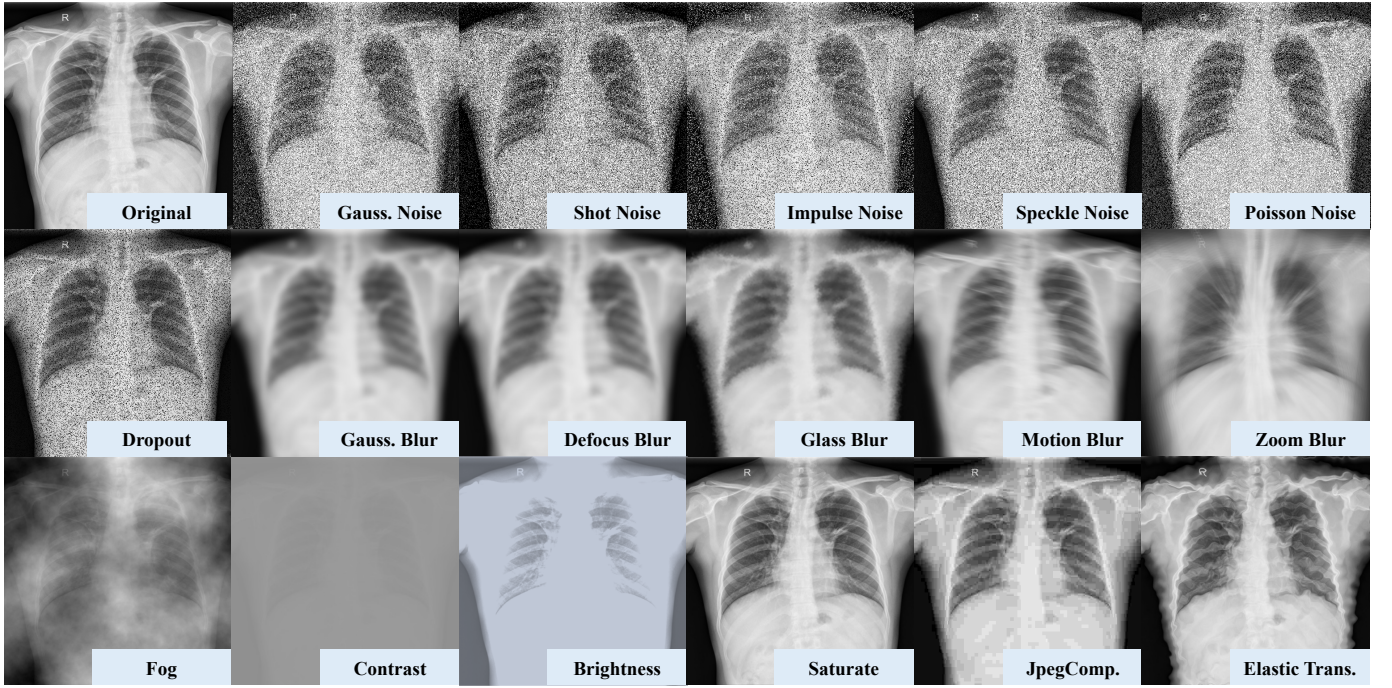


Fig. 2: The visualization of different data corruptions and perturbations. We choose these noises, blur, and digital transformations that are common in real-world applications for verification of the robustness of our model.

TABLE III: Comparison robustness performances among different data corruption in the lung segmentation task on MC dataset using PSPNet [23] as baseline. Dice is utilized as the evaluation metric.

Method	PSPNet (—)	PSPNet (+VAE)	PSPNet (+ImageNet)	PSPNet (+Jigsaw)	PSPNet (+MoCo)	PSPNet (+Ours)	Rec-PSPNet (—)	Rec-PSPNet (+MoCo)	Rec-PSPNet (+Ours)
Original	91.69 ± 0.1	95.73 ± 0.3	96.02 ± 0.3	96.03 ± 0.2	97.27 ± 0.2	95.98 ± 0.1	92.31 ± 0.2	97.04 ± 0.1	96.95 ± 0.2
Gauss. Noise	82.24 ± 0.3	83.41 ± 0.4	75.82 ± 0.2	73.29 ± 0.2	82.01 ± 0.4	94.14 ± 0.2	92.01 ± 0.3	88.78 ± 0.2	95.80 ± 0.3
Shot Noise	82.22 ± 0.3	69.53 ± 0.2	86.93 ± 0.2	85.75 ± 0.2	87.53 ± 0.1	94.19 ± 0.3	90.68 ± 0.2	89.53 ± 0.1	95.75 ± 0.1
Impulse Noise	72.48 ± 0.3	78.20 ± 0.1	72.63 ± 0.3	88.30 ± 0.2	78.90 ± 0.2	94.41 ± 0.1	92.19 ± 0.1	90.07 ± 0.2	95.83 ± 0.2
Speckle Noise	82.28 ± 0.2	84.81 ± 0.3	79.96 ± 0.1	72.78 ± 0.1	85.79 ± 0.2	94.02 ± 0.1	90.48 ± 0.1	91.03 ± 0.1	95.96 ± 0.2
Poisson Noise	71.18 ± 0.4	75.94 ± 0.1	78.96 ± 0.2	79.71 ± 0.1	86.20 ± 0.2	93.29 ± 0.3	91.24 ± 0.4	89.06 ± 0.2	95.06 ± 0.3
Dropout	82.60 ± 0.3	79.93 ± 0.3	78.50 ± 0.2	73.88 ± 0.4	86.56 ± 0.1	92.65 ± 0.3	90.55 ± 0.4	95.54 ± 0.1	95.33 ± 0.2
Gauss. Blur	80.10 ± 0.3	94.36 ± 0.4	85.99 ± 0.4	78.85 ± 0.1	76.19 ± 0.1	94.96 ± 0.4	91.59 ± 0.3	94.69 ± 0.1	96.25 ± 0.1
Glass Blur	82.19 ± 0.2	94.38 ± 0.1	83.39 ± 0.2	88.74 ± 0.4	90.75 ± 0.2	94.97 ± 0.2	92.17 ± 0.3	95.58 ± 0.1	96.03 ± 0.1
Defocus Blur	80.14 ± 0.1	94.54 ± 0.3	86.49 ± 0.3	80.63 ± 0.2	85.60 ± 0.2	95.07 ± 0.2	91.98 ± 0.3	92.75 ± 0.1	96.34 ± 0.2
Motion Blur	78.24 ± 0.3	88.39 ± 0.2	83.52 ± 0.1	85.22 ± 0.2	91.02 ± 0.4	89.48 ± 0.1	87.06 ± 0.3	89.34 ± 0.2	90.71 ± 0.3
Zoom Blur	76.68 ± 0.2	78.18 ± 0.3	85.07 ± 0.2	83.74 ± 0.3	88.41 ± 0.1	82.02 ± 0.1	82.95 ± 0.3	88.89 ± 0.1	84.68 ± 0.2
Fog	46.58 ± 0.3	51.37 ± 0.2	70.02 ± 0.2	70.89 ± 0.3	75.43 ± 0.1	67.74 ± 0.2	58.34 ± 0.2	76.55 ± 0.2	71.19 ± 0.2
Contrast	22.49 ± 0.4	49.04 ± 0.2	31.05 ± 0.2	41.39 ± 0.3	56.25 ± 0.2	47.78 ± 0.2	22.17 ± 0.3	57.66 ± 0.2	59.38 ± 0.1
Brightness	47.48 ± 0.2	72.33 ± 0.1	89.89 ± 0.2	87.94 ± 0.1	82.16 ± 0.2	75.62 ± 0.2	64.40 ± 0.3	91.50 ± 0.3	97.09 ± 0.2
Saturate	83.16 ± 0.2	95.73 ± 0.2	96.13 ± 0.2	96.03 ± 0.1	97.28 ± 0.1	95.98 ± 0.3	92.38 ± 0.3	97.43 ± 0.1	97.09 ± 0.2
JpegComp.	83.05 ± 0.2	95.75 ± 0.3	89.24 ± 0.3	90.86 ± 0.1	92.48 ± 0.1	95.80 ± 0.5	92.23 ± 0.3	92.36 ± 0.2	96.93 ± 0.4
Elastic Trans.	82.82 ± 0.4	95.17 ± 0.1	93.36 ± 0.4	93.20 ± 0.3	96.43 ± 0.5	95.60 ± 0.3	92.62 ± 0.1	94.16 ± 0.2	96.72 ± 0.2
Avg.	72.63	81.24	80.41	80.66	84.65	88.10	83.24	89.11	91.18
↓	18.46	14.49	15.61	15.37	12.62	07.88	09.07	07.93	05.77

↓ denotes that compared with the clean data (original) the average dice descent by.

adding the proposed reconstruction network on MC dataset. Yet, the main idea of this paper is not to boost the model performance on the clear and in-domain data. We pay more attention to the model's robustness and generalization.

Robustness. For visualization of the robustness result, we simulate different types of data corruptions and perturbations,

including noises, blurs, and digital translations, as shown in Fig.2. The robustness tests are conducted on the three target datasets (MC, JSRT, and SH) with two segmentation baselines (PSPNet and UNet). Data corruptions can be implemented with the imgaug library. The results of MC datasets are shown in Tables II and III. Table II and Table III show the

TABLE IV: Summary of model generalization performance on MC, JSRT, SH datasets (MC \rightarrow JSRT denotes training the network on MC dataset and directly testing on the JSRT dataset). Dice is utilized as the evaluation metric.

Method \ Dataset	MC \rightarrow MC	MC \rightarrow JSRT	MC \rightarrow SH	JSRT \rightarrow JSRT	JSRT \rightarrow MC	JSRT \rightarrow SH	SH \rightarrow SH	SH \rightarrow MC	SH \rightarrow JSRT	Avg.
UNet (—)	89.95 \pm 0.1	73.20 \pm 0.2	77.74 \pm 0.2	94.18 \pm 0.3	82.74 \pm 0.4	85.71 \pm 0.2	88.03 \pm 0.6	46.69 \pm 0.3	72.24 \pm 0.5	78.94
UNet (+VAE)	92.80 \pm 0.2	89.15 \pm 0.3	80.19 \pm 0.2	95.43 \pm 0.3	84.42 \pm 0.3	90.75 \pm 0.1	86.66 \pm 0.2	83.69 \pm 0.2	83.38 \pm 0.3	87.39
UNet (+Ours)	94.35 \pm 0.4	92.38 \pm 0.1	86.05 \pm 0.3	94.41 \pm 0.2	84.58 \pm 0.2	89.53 \pm 0.3	91.31 \pm 0.3	90.83 \pm 0.1	88.44 \pm 0.2	90.21
Rec-UNet (—)	92.87 \pm 0.3	82.52 \pm 0.1	75.26 \pm 0.3	95.07 \pm 0.2	91.19 \pm 0.1	89.43 \pm 0.4	89.34 \pm 0.3	78.26 \pm 0.4	82.51 \pm 0.1	88.55
Rec-UNet (+Ours)	95.98 \pm 0.1	94.87 \pm 0.1	91.65 \pm 0.3	96.56 \pm 0.4	95.86 \pm 0.1	96.00 \pm 0.2	93.17 \pm 0.6	89.48 \pm 0.2	90.35 \pm 0.3	93.78
PSPNet (—)	91.69 \pm 0.2	84.49 \pm 0.1	63.84 \pm 0.3	95.34 \pm 0.2	83.40 \pm 0.5	85.45 \pm 0.3	83.26 \pm 0.4	29.52 \pm 0.3	76.61 \pm 0.2	77.07
PSPNet (+SwAV)	95.65 \pm 0.3	92.18 \pm 0.1	90.97 \pm 0.6	95.80 \pm 0.2	94.33 \pm 0.5	71.43 \pm 0.2	91.34 \pm 0.1	60.97 \pm 0.3	67.83 \pm 0.2	84.72
PSPNet (+Color.)	91.94 \pm 0.1	85.97 \pm 0.3	85.03 \pm 0.2	94.25 \pm 0.3	92.48 \pm 0.2	88.63 \pm 0.4	86.63 \pm 0.6	85.23 \pm 0.1	79.93 \pm 0.4	87.79
PSPNet (+VAE)	95.73 \pm 0.2	92.98 \pm 0.1	84.87 \pm 0.3	94.26 \pm 0.1	89.00 \pm 0.3	87.56 \pm 0.2	91.97 \pm 0.3	78.53 \pm 0.2	86.86 \pm 0.3	89.08
PSPNet (+BYOL)	94.75 \pm 0.1	92.41 \pm 0.4	91.41 \pm 0.2	95.37 \pm 0.3	93.86 \pm 0.2	92.61 \pm 0.1	92.32 \pm 0.4	90.26 \pm 0.5	90.51 \pm 0.2	92.61
PSPNet (+RotNet)	95.94 \pm 0.2	93.98 \pm 0.1	92.19 \pm 0.2	96.20 \pm 0.4	93.41 \pm 0.1	92.43 \pm 0.4	93.00 \pm 0.5	91.06 \pm 0.2	89.16 \pm 0.3	93.04
PSPNet (+SimCLR)	95.62 \pm 0.3	92.92 \pm 0.1	92.72 \pm 0.5	95.88 \pm 0.1	94.55 \pm 0.4	94.04 \pm 0.2	93.29 \pm 0.3	90.74 \pm 0.2	91.48 \pm 0.1	93.47
PSPNet (+ImageNet)	96.02 \pm 0.1	94.40 \pm 0.5	94.56 \pm 0.2	96.54 \pm 0.3	95.26 \pm 0.2	94.24 \pm 0.2	92.67 \pm 0.3	91.07 \pm 0.1	90.89 \pm 0.3	93.96
PSPNet (+Jigsaw)	96.02 \pm 0.3	94.38 \pm 0.3	93.26 \pm 0.1	96.32 \pm 0.3	93.79 \pm 0.2	93.99 \pm 0.2	93.95 \pm 0.1	92.33 \pm 0.1	92.81 \pm 0.5	94.09
PSPNet (+MoCo)	97.27 \pm 0.1	95.01 \pm 0.1	94.71 \pm 0.4	96.50 \pm 0.2	95.61 \pm 0.3	94.49 \pm 0.3	94.75 \pm 0.3	93.22 \pm 0.2	92.47 \pm 0.1	95.00
PSPNet (+Ours)	95.98 \pm 0.2	93.90 \pm 0.3	90.92 \pm 0.1	96.24 \pm 0.5	93.80 \pm 0.1	92.15 \pm 0.2	92.68 \pm 0.1	90.61 \pm 0.5	89.67 \pm 0.3	92.88
Rec-PSPNet (—)	92.31 \pm 0.1	88.86 \pm 0.3	72.66 \pm 0.1	95.51 \pm 0.6	86.02 \pm 0.4	84.60 \pm 0.2	85.17 \pm 0.5	56.60 \pm 0.2	71.87 \pm 0.3	81.51
Rec-PSPNet (+MoCo)	97.04 \pm 0.2	95.56 \pm 0.1	94.63 \pm 0.2	96.80 \pm 0.1	96.30 \pm 0.2	94.53 \pm 0.2	94.80 \pm 0.2	94.68 \pm 0.1	90.10 \pm 0.2	94.94
Rec-PSPNet (+Ours)	96.95 \pm 0.3	95.69 \pm 0.2	95.05 \pm 0.2	97.19 \pm 0.1	96.23 \pm 0.1	95.02 \pm 0.2	95.77 \pm 0.1	92.45 \pm 0.2	92.82 \pm 0.3	95.23

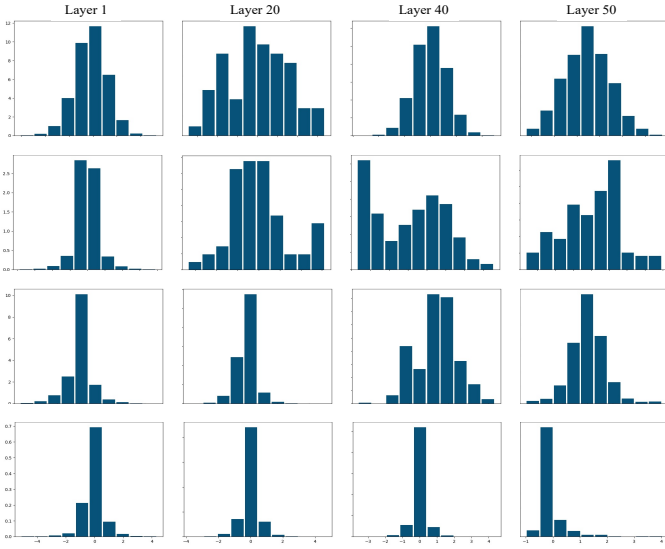


Fig. 3: The visualization of the network’s weights distribution. Each column denotes one layer weights of ResNet-50. The first row shows weights trained from scratch; the second row is model trained with the ImageNet pretrained model; the third one is the MoCo; the last row is the T-AE.

segmentation metric (dice) of the UNet-based networks and PSPNet-based networks, respectively. Taking Table I III as an example, in the head row, PSPNet (—) denotes the training the PSPNet from scratch and PSPNet (MoCo) is using the MoCo pretraining method, etc. The original (the first row) represents the segmentation performance on the original clean data. while other rows show the result of these methods testing on different data corruptions. The last row provides the average dice among all corruptions and their decrease. Compared with training from scratch or recent pretraining models, such as VAE [27],

classification on ImageNet [10], Jigsaw [11], and MoCo [17], our proposed segmentation framework achieves the superior or comparable performance, such as our final framework (**Rec-PSPNet** with T-AE pretraining) outperforms the MoCo by 2.07% and the **Rec-PSPNet** by 7.94%. In addition, compared with the vanilla PSPNet, the T-AE pretraining achieves a 15.47% improvement, and **Rec-PSPNet** can get a 10.61% improvement. These results show both the reconstruction branch (**Rec-**) and the proposed pretraining method (T-AE) are effective. Due to the limited page length, results of JSRT and SH datasets are reported in ³. Moreover, we visualize the sparsity of the model weight in Fig. 3. It is well-known that a degree of sparsity can encourage the model to be more robust. From left to right, we show the histograms of four hidden layers (layer 1, 20, 40, and 50) weights from shallow to deep. Compared with training from scratch, pretrained on classification ImageNet [10], and MoCo [17], weights are sparser with our proposed T-AE.

Generalization. The generalization tests are conducted on the three target datasets. The experiment setting is that we select one dataset for training and the others for testing. For example, the model trained on MC dataset is tested on MC (MC \rightarrow MC), JSRT (MC \rightarrow JSRT), and SH (MC \rightarrow SH) dataset, respectively. Baseline networks are UNet [20] and PSPNet [23]. As shown in Table IV, we compare our proposed pretraining technique with training from scratch, SwAV [14], colorizing gray-scale images (Color.) [12], VAE [27], BYOL [15], RotNet [13], SimCLR [16], classification on ImageNet [3], Jigsaw [11], MoCo [17]. The pretrained model for PSPNet is ResNet-50 so that we can utilize the public pretrained model of their algorithms. And due to the backbone of UNet is not the standard ResNet-50, we cannot load these pretrained models. The generalization performances are reported in Table IV. The

³Results of JSRT and SH datasets

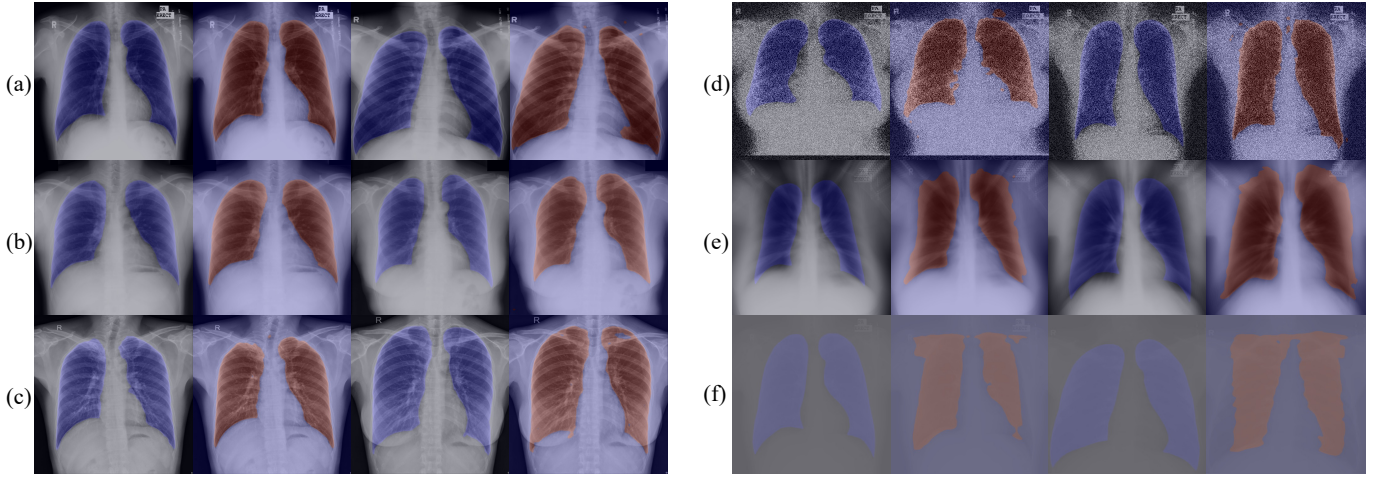


Fig. 4: The visualization of segmentation results. The blue region denotes the mask, and the red area is the predicted result. The model is trained on the MC dataset, then tests on the MC validation set (a); the JSRT dataset (b); the SH dataset (c); the Poisson noised MC dataset (d); the zoom blurred MC dataset (e); the contrast transformed MC dataset (f).

same conclusion can be summarized from this table that both the proposed pretraining method and the reconstruction branch can improve the model performance. We can see that the performances of our model are consistent when testing on other unseen datasets, while others drop a lot. For example, the PSPNet trained from the scratch has a 91.69% dice on the MC dataset while only having a 63.84% dice when directly applied to the SH dataset; however, the PSPNet with our reconstruction network (**Rec-PSPNet**) gets a 92.31% dice on the MC dataset and has 72.66% dice when directly applied to the SH dataset; the PSPNet with our proposed pretrained model gets a 95.98% dice on the MC dataset and keeps a stable 90.92% dice when directly applied to the SH dataset; The PSPNet trained with SwAV[14] as the pretrained model achieves a 91.34% dice on the SH dataset while only having a 67.83% dice when directly applied to the JSRT dataset; however, the PSPNet with our proposed pretrained model and the reconstruction network has a 95.77% dice on the SH dataset and maintains a 92.82% dice when directly applied to the JSRT dataset; Our final frameworks (**Rec-PSPNet** or UNet with T-AE weights) achieve 95.13% and 93.78% average dice, respectively. Compared with the baseline (PSPNet and UNet), an improvement of 18.06% and 14.84% is got. Our proposed pretraining method also outperforms the MoCo under the same condition. In a nutshell, the result proves the effectiveness of our proposed pretraining method and the reconstruction branch.

In the end, we visualize the segmentation results of our proposed framework (the **Rec-PSPNet** with T-AE pretrained model) in Fig. 4. The model is only finetuned on the clean MC data (denoted as Fig. 4 (a)), the generalized segmentation visualization on the other two datasets (the JSRT and the SH dataset) is shown in Fig. 4 (b-c). We can see that the model can segment the lung area well even it does not see the data during the training phase. Moreover, the robust segmentation results are shown in Fig. 4 (d-f). Our proposed method shows good robustness to the data corruptions, such as Poisson noise, zoom blur, and contrast variance.

TABLE V: Comparison robustness performances among different number of tiles (N) on the MC dataset with **Rec-UNet**.

N	1	4	9	16
Gauss. Noise	91.71 \pm 0.3	93.23 \pm 0.3	93.47 \pm 0.2	92.15 \pm 0.2
Shot Noise	90.41 \pm 0.4	95.86 \pm 0.2	94.33 \pm 0.3	92.84 \pm 0.2
Gauss. Blur	88.53 \pm 0.3	93.46 \pm 0.2	95.55 \pm 0.3	94.05 \pm 0.3
Glass Blur	88.74 \pm 0.3	95.16 \pm 0.2	95.28 \pm 0.3	91.26 \pm 0.3
Contrast	54.08 \pm 0.5	61.29 \pm 0.2	63.50 \pm 0.2	64.04 \pm 0.4
Saturate	92.26 \pm 0.2	94.60 \pm 0.2	94.67 \pm 0.3	94.59 \pm 0.3

D. Ablation Study

Effect of the number of tiles. One of the most important factors of the proposed T-AE is the number of patches. In the experiment section, we divide an image into 9 patches. Here, we test the model robustness performance with the number of tiles from 1 to 4, 9, and 16. We select 6 different data corruptions, i.e. adding Gaussian noise, shot noise, Gaussian blur, glass blur, changing the contrast and the saturate. The experiment result is reported in Table V. We can see that the model with the number of tiles 4, 9, and 16 is quite stable. The number of tiles equals 1 means training the network with the whole image, i.e. the T-AE becomes the sliced-Wasserstein autoencoder, so when the model performance drops a lot when $N = 1$. Considering the performance and the computational cost when increasing the number of tiles, we finally divide the image into 9 non-overlapping patches.

Effect of the data corruption level. We investigate the level of the data corruptions on the MC, the JSRT, and the SH dataset. In particular, five data corruptions, including adding Gaussian noise, Poisson noise, zoom blur, fog, and changing the contrast are shown in Fig. 5. As the corruption level increases, the performance of the baseline method i.e. the PSPNet trained from scratch, degrades drastically (denoted by the blue line in Fig. 5), while our proposed method, i.e. the PSPNet only with our T-AE pretrained model as shown

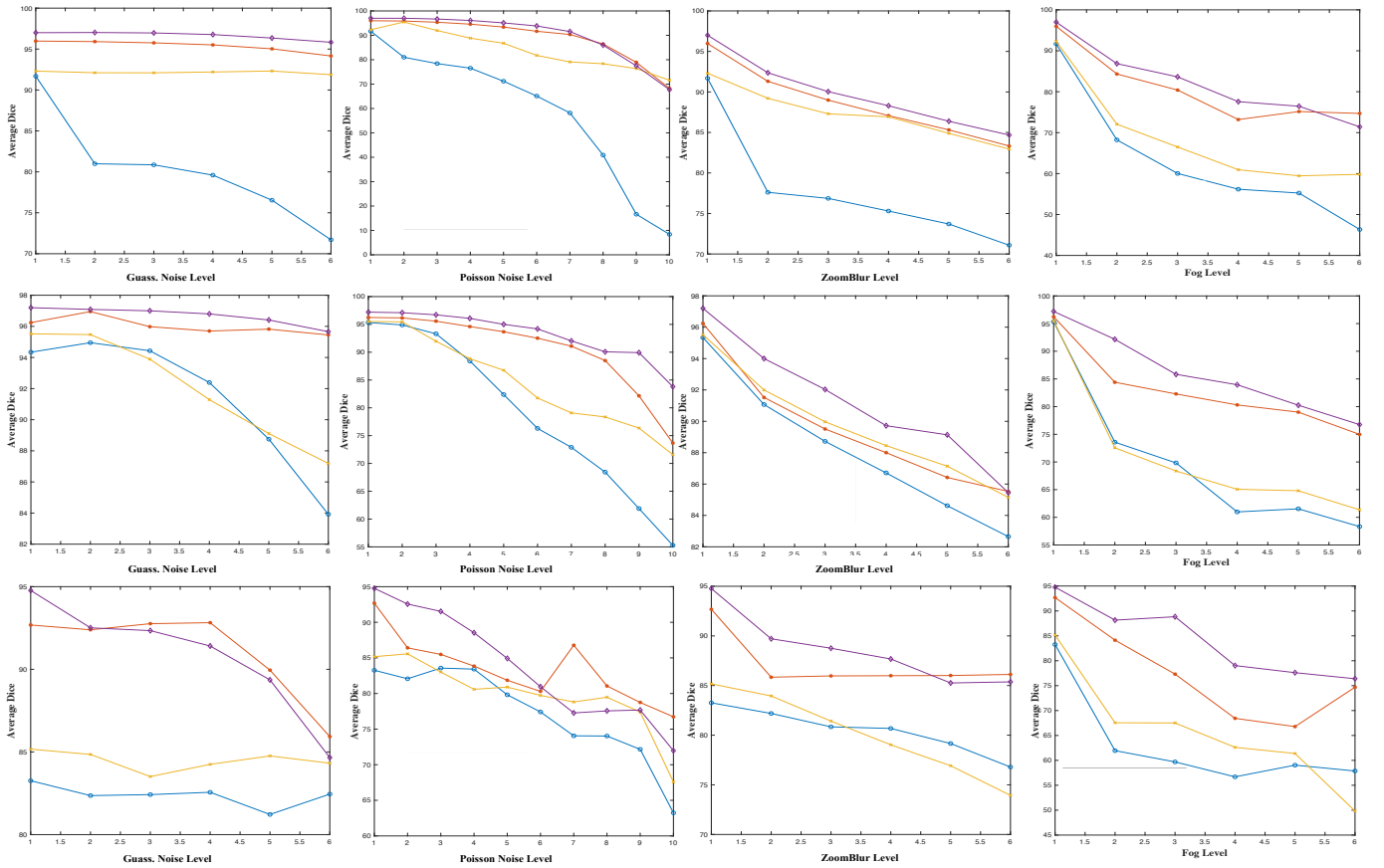


Fig. 5: The robustness performance comparison between our proposed method and baselines on different data corruption. The first row is the result on the MC dataset; the second row is the JSRT; the third row is the SH.

TABLE VI: Summary of model generalization performance in the lung segmentation task under the few-shot learning condition on MC, JSRT, SH X-ray datasets. Dice is utilized as the evaluation metric.

Dataset		MC → MC	MC → JSRT	MC → SH	JSRT → JSRT	JSRT → MC	JSRT → SH	SH → SH	SH → MC	SH → JSRT	Avg.
Method											
Labeled 2%	PSPNet (—)	65.24 ± 0.3	55.93 ± 0.2	37.51 ± 0.2	71.07 ± 0.2	57.28 ± 0.3	49.53 ± 0.1	61.94 ± 0.3	25.26 ± 0.3	52.90 ± 0.2	52.96
	PSPNet (+Ours)	75.12 ± 0.1	80.25 ± 0.1	70.78 ± 0.2	81.90 ± 0.2	75.01 ± 0.2	73.33 ± 0.1	68.54 ± 0.1	70.26 ± 0.2	72.64 ± 0.1	74.20
	Rec-PSPNet (—)	68.56 ± 0.1	71.03 ± 0.1	61.05 ± 0.2	69.14 ± 0.3	61.14 ± 0.2	63.76 ± 0.2	60.42 ± 0.1	40.39 ± 0.3	56.74 ± 0.3	61.36
	Rec-PSPNet (+Ours)	75.90 ± 0.1	80.39 ± 0.2	73.57 ± 0.2	83.28 ± 0.1	74.06 ± 0.2	76.70 ± 0.1	90.26 ± 0.2	88.39 ± 0.2	88.87 ± 0.1	81.27
Labeled 5%	PSPNet (—)	73.75 ± 0.2	74.71 ± 0.2	56.82 ± 0.3	74.02 ± 0.2	64.06 ± 0.3	59.41 ± 0.2	63.84 ± 0.2	28.39 ± 0.3	58.80 ± 0.2	61.53
	PSPNet (+Ours)	81.78 ± 0.2	84.77 ± 0.3	74.26 ± 0.3	84.83 ± 0.2	76.77 ± 0.1	78.08 ± 0.2	72.34 ± 0.2	53.72 ± 0.3	73.40 ± 0.3	75.55
	Rec-PSPNet (—)	76.26 ± 0.1	70.58 ± 0.2	64.52 ± 0.2	76.82 ± 0.2	66.70 ± 0.3	72.37 ± 0.3	71.55 ± 0.2	48.45 ± 0.2	66.74 ± 0.1	68.22
	Rec-PSPNet (+Ours)	82.91 ± 0.1	84.73 ± 0.1	79.58 ± 0.2	85.64 ± 0.2	79.30 ± 0.1	80.52 ± 0.1	90.04 ± 0.1	88.10 ± 0.1	88.01 ± 0.1	84.31
Labeled 7%	PSPNet (—)	77.58 ± 0.2	76.28 ± 0.3	59.43 ± 0.1	81.83 ± 0.3	66.87 ± 0.3	75.20 ± 0.2	81.83 ± 0.3	32.49 ± 0.2	61.86 ± 0.2	68.15
	PSPNet (+Ours)	84.72 ± 0.2	84.75 ± 0.1	74.73 ± 0.2	88.70 ± 0.1	81.88 ± 0.1	82.78 ± 0.3	73.76 ± 0.2	73.70 ± 0.1	71.21 ± 0.2	79.58
	Rec-PSPNet (—)	76.69 ± 0.1	79.69 ± 0.2	64.72 ± 0.2	83.89 ± 0.3	75.13 ± 0.3	75.18 ± 0.2	91.01 ± 0.2	65.09 ± 0.1	90.53 ± 0.2	77.99
	Rec-PSPNet (+Ours)	87.00 ± 0.1	86.43 ± 0.2	81.14 ± 0.1	89.45 ± 0.2	87.45 ± 0.1	84.59 ± 0.1	92.01 ± 0.1	91.35 ± 0.2	91.42 ± 0.1	87.87
Labeled 10%	PSPNet (—)	79.04 ± 0.3	71.61 ± 0.2	63.41 ± 0.1	86.03 ± 0.4	72.19 ± 0.2	76.62 ± 0.2	74.40 ± 0.3	24.63 ± 0.2	60.12 ± 0.1	67.56
	PSPNet (+Ours)	87.20 ± 0.1	88.51 ± 0.2	80.39 ± 0.1	91.00 ± 0.1	84.81 ± 0.2	84.30 ± 0.3	84.90 ± 0.3	86.97 ± 0.1	89.32 ± 0.3	86.01
	Rec-PSPNet (—)	84.90 ± 0.2	82.83 ± 0.1	78.54 ± 0.2	89.55 ± 0.4	71.22 ± 0.2	78.57 ± 0.3	90.06 ± 0.2	60.86 ± 0.1	72.90 ± 0.3	78.83
	Rec-PSPNet (+Ours)	87.46 ± 0.2	89.26 ± 0.1	82.49 ± 0.2	95.80 ± 0.2	91.74 ± 0.1	89.66 ± 0.1	92.43 ± 0.2	90.18 ± 0.2	90.37 ± 0.2	89.93

with the red line, the PSPNet only with our reconstruction network (**Rec-PSPNet**) as shown with the yellow line, and the final framework (**Rec-PSPNet** with T-AE pretrained model) as shown with purple line can maintain the accuracy under different level corruptions. The comparisons between the baseline demonstrate the effectiveness of our proposed pretraining method and the reconstruction branch.

Effect of the number of the training data. Table IV shows results under the few-shot learning conditions. We leverage the PSPNet as the baseline and compare the model generalization performance under the ratio of the training data is only 2%, 5%, 7%, and 10%. Even the training set is limited, our proposed framework shows superior results.

E. Discussion

In the experiment section, comprehensive results demonstrate the outstanding robustness and generalization of our proposed framework. Quantitative experiments of robustness (Table II, III) show that both our proposed pretraining method (T-AE) and the reconstruction branch can improve the model's robustness. Likewise, results (Table IV) prove that our proposed methods can achieve superior generalization performance. In addition, Table VI shows our proposed methods boost the model performance under the limited data scale condition. The effectiveness of each part is also can be seen in these tables. In conclusion, we can answer the problems presented in the introduction (i) pretraining can improve the model performance, furthermore, it contributes to the model robustness and generalization; (ii) utilizing the ImageNet pretrained models is inferior when the target domain is significantly different.

V. CONCLUSION

In this paper, we investigate the effect of the pretraining, such as the model performance of using the ImageNet pretrained models and using the domain data-based pretrained model. Not only focus on the training accuracy but the robustness and generalization capability is studied. Furthermore, we propose a two-stage robust generalized medical image segmentation framework. In particular, we design a novel pretraining method (T-AE) for pretraining on the domain-related data to learn meaningful representations and domain knowledge. Then the downstream segmentation network coupled with a reconstruction branch is designed. Quantitative experiments of robustness and generalization demonstrate the validity of each of our proposed methods.

REFERENCES

- [1] I. Goodfellow, Y. Bengio, A. Courville, et al, *Deep learning*. MIT press, 2016.
- [2] S. M. McKinney, M. Sieniek, V. Godbole, et al., "International evaluation of an AI system for breast cancer screening," *Nature*, vol. 577, no. 7788, pp. 89-94, 2020.
- [3] J. Deng, W. Dong, R. Socher, et al, "Imagenet: A large-scale hierarchical image database," in *IEEE Conference on Computer Vision and Pattern Recognition (CVPR)*, pp. 248-255, 2009.
- [4] B. Zhou, A. Lapedriza, A. Khosla, et al, "Places: A 10 million image database for scene recognition," in *IEEE Transactions on Pattern Analysis and Machine Intelligence*, 2017.
- [5] T. Dissanayake, T. Fernando, S. Denman, H. Ghaemmaghami, S. Sridharan and C. Fookes, "Domain generalization in biosignal classification," in *IEEE Transactions on Biomedical Engineering*, vol. 68, no. 6, pp. 1978-1989, 2021.
- [6] H. Li, Y. Wang, R. Wan, S. Wang, T. Q. Li, and A. C. Kot, "Domain generalization for medical imaging classification with linear-dependency regularization," in *Conference on Neural Information Processing Systems (NeurIPS)*, 2020.
- [7] A. V. Opbroek, M. A. Ikram, M. W. Vernooij and M. D. Bruijine, "Transfer learning improves supervised image segmentation across imaging protocols," in *IEEE Transactions on Medical Imaging*, vol. 34, no. 5, pp. 1018-1030, 2015.
- [8] N. Tajbakhsh, J. Y. Shin, S. R. Gurudu, R. T. Hurst, C. B. Kendall, M. B. Gotway, and J. Liang, "Convolutional neural networks for medical image analysis: full training or fine tuning?," in *IEEE Transactions on Medical Imaging*, vol. 35, no. 5, pp. 1299-1312, 2016.
- [9] K. He, R. Girshick, and P. Dollar, "Rethinking imagenet pre-training," in *International Conference on Computer Vision (ICCV)*, 2019.
- [10] K. He, X. Zhang, S. Ren, and J. Sun, "Deep residual learning for image recognition," in *IEEE Conference on Computer Vision and Pattern Recognition (CVPR)*, pp. 770-778, 2016.
- [11] M. Noroozi and P. Favaro, "Unsupervised learning of visual representations by solving jigsaw puzzles," in *European Conference on Computer Vision (ECCV)*, pp. 69-84, 2016.
- [12] R. Zhang, P. Isola, and A. A. Efros, "Colorful image colorization," in *European Conference on Computer Vision (ECCV)*, 2016.
- [13] S. Gidaris, P. Singh, N. Komodakis, "Unsupervised representation learning by predicting image rotations," in *International Conference on Learning Representations (ICLR)*, 2018.
- [14] M. Caron, I. Misra, J. Mairal, et al., "Unsupervised learning of visual features by contrasting cluster assignments," in *Neural Information Processing Systems (NeurIPS)*, 2020.
- [15] J. B. Grill, F. Strub, F. Altché, et al., "Bootstrap your own latent: A new approach to self-supervised learning," in *Neural Information Processing Systems (NeurIPS)*, 2020.
- [16] T. Chen, S. Kornblith, M. Norouzi, et al., "A simple framework for contrastive learning of visual representations," in *International Conference on Machine Learning (ICML)*, pp. 1597-1607, 2020.
- [17] K. He, H. Fan, Y. Wu, et al., "Momentum contrast for unsupervised visual representation learning," in *IEEE Conference on Computer Vision and Pattern Recognition (CVPR)*, pp. 9729-9738, 2020.
- [18] D. Hendrycks, K. Lee, and N. Mazeika, "Using pre-training can improve model robustness and uncertainty," in *International Conference on Machine Learning (ICML)*, 2019, pp. 2712-2721.
- [19] H. Sowrirajan, J. Yang, A. Y. Ng, and P. Rajpurkar, "MoCo-CXR: MoCo pretraining improves representation and transferability of chest X-ray models," in *International Conference on Medical Imaging with Deep Learning (MIDL)*, 2021.
- [20] O. Ronneberger, P. Fischer, and T. Brox, "U-net: Convolutional networks for biomedical image segmentation," in *International Conference on Medical Image Computing and Computer-assisted Intervention*, pp. 234-241, 2015.
- [21] L. Zhang, A. Liu, J. Xiao and P. Taylor, "Dual encoder fusion U-Net (DEFU-Net) for cross-manufacturer chest X-ray segmentation," in *International Conference on Pattern Recognition (ICPR)*, pp. 9333-9339, 2021.
- [22] C. Chen, Y. Zhu, G. Papandreou, et al., "Encoder-decoder with atrous separable convolution for semantic image segmentation," in *European conference on computer vision (ECCV)*, pp. 801-818, 2018.
- [23] H. Zhao, J. Shi, X. Qi, X. Wang, and J. Jia "Pyramid scene parsing network," in *IEEE Conference on Computer Vision and Pattern Recognition (CVPR)*, pp. 2881- 2890, 2017.
- [24] R. Rashid, M. U. Akram, and T. Hassan, "Fully convolutional neural network for lungs segmentation from chest X-rays," in *International Conference Image Analysis and Recognition (ICIAR)*, pp. 71-80, 2018.
- [25] S. Candemir, S. Jaeger, K. Palaniappan K, et al., "Lung segmentation in chest radiographs using anatomical atlases with nonrigid registration," in *IEEE Transactions on Medical Imaging*, vol.33, no. 2, pp. 577-590, 2013.
- [26] I. Goodfellow, J. Pouget-Abadie, M. Mirza, B. Xu, D. Warde-Farley, S. Ozair, A. Courville, and Y. Bengio, "Generative adversarial nets," in *Conference on Neural Information Processing Systems (NeurIPS)*, 2014.
- [27] D. P. Kingma, and M. Welling, "Auto-Encoding variational Bayes," in *International Conference on Machine Learning (ICML)*, 2014.
- [28] T. W. Cenggoro, "Deep learning for imbalance data classification using class expert generative adversarial network," *Procedia Computer Science*, vol. 135, pp. 60-67, 2018.
- [29] A. Newell, J. Deng, "How useful is self-supervised pretraining for visual tasks?" in *IEEE Conference on Computer Vision and Pattern Recognition (CVPR)*, 2020, pp. 7345-7354.
- [30] I. Tolstikhin, O. Bousquet, S. Gelly, et al., "Wasserstein auto-encoders," in *International Conference on Learning Representation (ICLR)*, 2018.
- [31] S. Kolouri, G. Rohde, H. Hoffmann, "Sliced wasserstein distance for learning Gaussian mixture models," in *Computer Vision and Pattern Recognition (CVPR)*, 2018, pp. 3427-3436.
- [32] F. Milletari, N. Navab, S. A. Ahmadi, "V-net: Fully convolutional neural networks for volumetric medical image segmentation," in *International Conference on 3D Vision (3DV)*, 2016.
- [33] S. D. Kermany, M. Goldbaum, W. Cai, et al., "Identifying medical diagnoses and treatable diseases by image-based deep learning," *Cell*, vol. 172, np. 5, pp. 1122-1131, 2018.
- [34] S. Jaeger, S. Candemir, S. Antani, et al., "Two public chest X-ray datasets for computer-aided screening of pulmonary diseases," *Quant Imaging Med Surg*, vol. 4, no. 6, pp. 475-477, 2014.
- [35] J. Shiraishi, S. Katsuragawa, J. Ikezoe et al., "Development of a digital image database for chest radiographs with and without a lung nodule: Receiver operating characteristic analysis of radiologists' detection of pulmonary nodules." *AJR*, vol. 174, pp. 71-74, 2000.